Effects of a Conducting Wall on Z-Pinch Stability

Sean D. Knecht, Weston Lowrie, and Uri Shumlak

***Abstract*— The stabilizing effect of a conducting wall on Z-pinch stability has been investigated through a systematic experimental and numerical study. Numerical simulations of a Z-pinch with a cylindrical conducting wall are compared with a case that modeled perforations in the conducting wall. The conducting wall also acts as the return current path for these investigations. Plasma conditions with various pinch sizes were studied numerically to better understand the effect of wall stabilization in Z-pinches. A study using the ZaP Flow Z-Pinch was performed by inserting a 0.35-m perforated section of electrode that has eight longitudinal slots cut from the outer electrode, reducing the conducting wall material by ≈70%. This modification prevents currents from flowing freely along the azimuthal distance of the outer electrode required to stabilize the $m = 1, 2, 3$ modes, which are experimentally monitored. Operating with identical experimental parameters with and without the perforated electrode was assumed to produce similar equilibrium and flow shear conditions in the pinch. Comparing the stability characteristics isolated the potential effects of the conducting wall. Magnetic data, interferometry, and optical images indicate that the conducting wall does not have a discernible effect on stability in the ZaP experiment. This result agrees with simulations with similar ratios of conducting wall radius to pinch radius.**

***Index Terms*— Magnetohydrodynamics (MHD), wall stabilization, Z-pinch.**

I. INTRODUCTION

CLOSE-FITTING, conducting walls have been observed to provide stability in a variety of magnetic confinement configurations. Early experimental work with arc sources in high-temperature gases found a close-fitting wall provides stability [1], [2]. Subsequently, early arcjet research in the 1960s established wall stabilization techniques empirically [3] and many early designs used a constrictor as a wall stabilization technique [4]–[10]. Much of this early work focused on finding optimal parameters to operate arcjets as rocket engines, while changing the constrictor diameter, input power, breakdown voltage, gas flow, and so on.

The wall stabilization techniques developed throughout the gas arc and arcjet research were extended in research directed toward fusion energy to Z-pinches and theta pinches [11]–[16], and a more theoretical understanding of the phenomenon was established. Later research in [17] using a linear stability analysis found that a close-fitting conducting wall around a diffuse pinch provides complete stability provided, $r_w/a < 1.2$, where r_w is the radius of the conducting wall and a is the pinch radius. When the wall is moved beyond this threshold distance from the pinch, the wall no longer stabilizes the plasma.

Wall stabilization has also been observed in tokamaks, for example [18] and [19], and can increase attainable values of β. Given a proper geometry, a close-fitting conducting wall stabilizes the tilt and shift modes in spheromaks [20], [21].

In this paper, we will present the results of a systematic experimental and numerical study to investigate the effects of a conducting wall on Z-pinch stability. Our results support the conclusion that a conducting wall must be in close proximity to the pinch boundary to provide a stabilizing effect, as predicted by linear stability analysis, and has no discernible effect on the stability on the ZaP Flow Z-Pinch. An experimental modification was made on the ZaP Flow Z-Pinch [22], [23] to evaluate the effects of the conducting wall on the stability of the pinch. This conducting wall also acts as the return current path in ZaP. The present hypothesis is that sheared axial flows are primarily responsible for stability in ZaP. The design of the ZaP Flow Z-Pinch is such that, according to linear stability analysis, the conducting wall is located far enough from the pinch to prevent any stabilizing effects. If the conducting wall is having a significant effect, then it would become apparent during the expected transition to instability as the flow shear decreases. Any stabilizing effect of a conducting wall was isolated by performing duplicate experiments with a conducting wall with eight azimuthally-spaced slots, with long axial extent, as shown in Fig. 2, reducing the conducting wall area by ≈70%.

The motivation for this modification was to reduce the azimuthal distance that current can flow along the outer conductor. The outer conductor in a Z-pinch conserves magnetic flux produced by plasma current and it can generate image currents to maintain pinch symmetry against perturbations. These image currents must have the same mode structure as the plasma perturbations to produce a stabilizing effect. This is a consequence of the exclusion of magnetic fields by a conductor. A z-component of magnetic field will be present at the wall if a kink mode develops. An azimuthal current is produced to cancel this field at the surface [24]. This current must necessarily produce a magnetic field with an identical

---

Manuscript received June 12, 2013; revised December 11, 2013 and March 31, 2014; accepted April 17, 2014. Date of publication May 16, 2014; date of current version June 6, 2014. This work was supported in part by the Department of Energy, in part by the U.S. Air Force Office of Scientific Research, and in part by the National Nuclear Security Administration.

S. D. Knecht was with the University of Washington, Seattle, WA 98195-2250 USA. He is now with the Applied Research Laboratory, Pennsylvania State University, University Park, PA 16801 USA (e-mail: sdk149@psu.edu).

W. Lowrie was with the University of Washington, Seattle, WA 98195-2250 USA. He is now with Applied Research Associates, Inc., Nashua 03060, U.K. (e-mail: wlowrie@ara.com).

U. Shumlak is with the Aerospace and Energetics Research Program, University of Washington, Seattle, WA 98195-2250 USA (e-mail: shumlak@uw.edu).

Color versions of one or more of the figures in this paper are available online at http://ieeexplore.ieee.org.

Digital Object Identifier 10.1109/TPS.2014.2320923

mode structure to the perturbation. For an $m = 1$ kink mode, the azimuthal image currents must flow freely around half of the circumference of the conducting wall. Similar behavior is observed in toroidal geometries in which eddy currents generated in conducting walls have the same mode structure as instabilities [25]. A conducting wall with eight longitudinal slots should prevent azimuthal current flow that would stabilize the $m = 1, 2, 3$ modes. The remaining conducting rods would support azimuthal currents around them, but any effect would be localized to the rod locations.

The equilibrium and flow shear conditions were assumed to be similar with and without the perforated section by operating the experiment with similar experimental conditions, isolating the effect of the conducting wall. The stabilizing effects of the conducting wall as flow shear decreases were then directly compared.

A concurrent computational study was undertaken using the HiFi [26]–[28] code to model a 3-D Z-pinch configuration, without sheared axial flows, with and without a perforated conducting wall section to better understand the stability effects of a conducting wall on a Z-pinch. The Z-pinch $m = 1$ kink mode was explored as a verification of the HiFi code and the HiFi code's multiblock geometry framework that makes nonaxisymmetric geometries possible. Experimental parameters were used in the simulations and the simulation results were compared with a linear stability analysis. The combined experimental and computational findings support the predictions of linear stability analysis regarding the required proximity of the conducting wall to the pinch.

II. Z-PINCH BACKGROUND AND $m = 1$ KINK MODE

The Z-pinch is a 1-D plasma confinement configuration with a purely azimuthal magnetic field and axial current density [29]. The name is derived from the fact that current flows in the axial $\hat{z}$ direction. An equilibrium can be obtained by solving the radial force balance equation

$$\frac{d}{dr}\left(p + \frac{B_\theta^2}{2\mu_0}\right) + \frac{B_\theta^2}{\mu_0 r} = 0 \tag{1}$$

where r is the radial dimension, p is the pressure, B_θ is the azimuthal magnetic field, and μ_0 is the permeability of free space. This equation represents the balance between magnetic forces and plasma pressure forces.

The Z-pinches are classically unstable to the $m = 1$ kink mode instability, which is well known both theoretically and experimentally [17], [30]–[34]. In contrast to the screw pinch or other configurations that have field-aligned current, the $m = 1$ kink mode in a Z-pinch is a pressure-driven instability. The kink mode instability grows when a locally higher magnetic field is experienced on one side of the pinch and the resulting increased magnetic pressure pushes the plasma fluid in one direction. A schematic of this phenomenon is shown in Fig. 1. The instability's growth rate can be predicted by linear stability analysis [17], [35]. For conditions found on ZaP, these growth rates are calculated to be on the order of 10 ns [22].

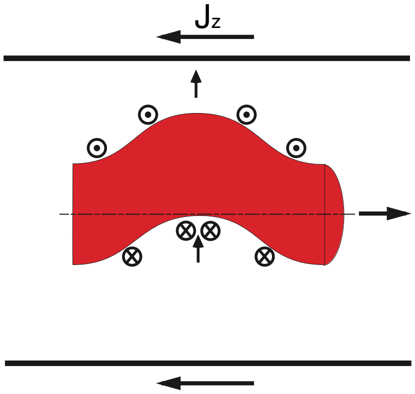

Fig. 1. Schematic diagram showing how locally higher magnetic field on one side of a Z-pinch leads to the $m = 1$ kink instability. The $\otimes$ symbol indicates azimuthal magnetic field directed into the page and the $\odot$ symbol indicates azimuthal magnetic field directed out of the page. Arrows indicated the upward direction of the net force.

III. ZAP FLOW Z-PINCH EXPERIMENTAL CONFIGURATION

The ZaP Flow Z-Pinch experiment is shown in Fig. 2 and consists of coaxial electrodes with no bias magnetic fields, similar to a Marshall gun design [36]. The outer electrode extends beyond the end of the inner electrode and acts as a pinch assembly region. Neutral gas is injected radially from the inner and outer electrodes and capacitor banks are discharged across the inner electrode and the outer conducting wall, ionizing the gas. Lorentz forces accelerate the plasma axially until it reaches the end of the inner electrode where the pinch assembles on the machine axis. The current sheet continues along the outer electrode until it reaches the end wall where the assembly is completed resulting in a pinch with a long axial extent ($\geq$1 m) and an embedded axial flow. The arrows in the top figure indicate the positions of the current sheet and direction of current flow immediately after ionization (green) and after pinch formation (yellow).

The hypothesis is that the Z-pinches produced remain stable as a result of sheared axial flows that are generated during the pinch formation process. Instability growth times for static plasmas with similar plasma and magnetic field parameters are on the order of 10 ns [37]. Stability of the pinch is observed for 1000s of times longer than the instability growth times [38]. A relationship exists between the existence of sheared axial flows and plasma stability in ZaP [37]. Specifically, stability is maintained when $dv_z/dr \geq 0.1 k_z V_A$, where dv_z/dr is the sheared axial flow, k_z is the axial wavenumber of the instability, and V_A is Alfvén velocity. The potential effects of a conducting wall on plasma stability in ZaP have not previously been investigated.

The ZaP operational parameters are shown in Table I. The experiment can be configured with inner electrodes of either 0.05- or 0.08-m radius and a 0.10-m radius outer electrode.

The experiment was modified to test the effects of the conducting wall, which also provides the return current path, on the pinch stability. A conducting wall produces a stabilizing effect on the kink mode by supporting azimuthal currents along the outer electrode circumference. For part of

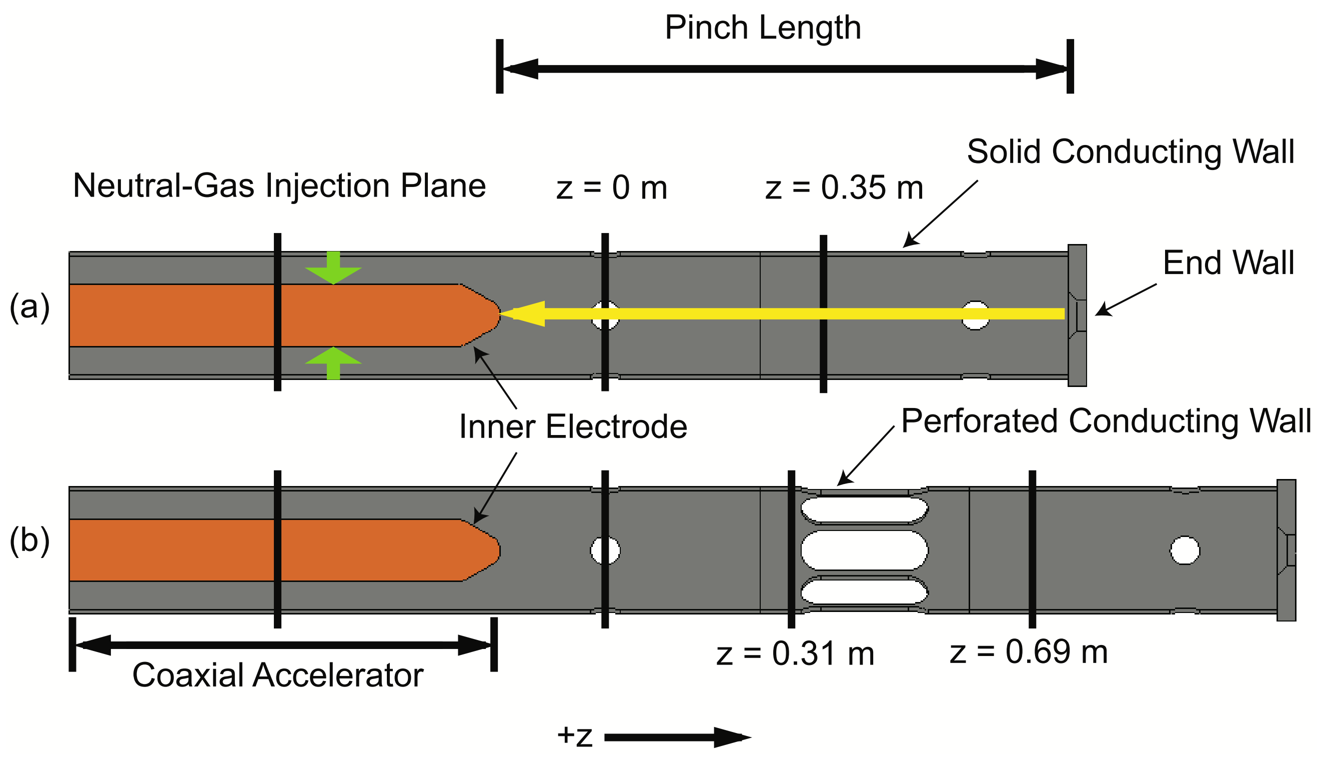

Fig. 2. Schematic view of ZaP experimental configurations used to evaluate effects of a conducting wall on plasma stability. (a) ZaP without the perforated electrode extension consists of a coaxial accelerator without bias magnetic fields coupled to a pinch assembly region. Inner electrodes with outer radius of either 0.05 or 0.08 m can be used; the inner radius of the solid conducting wall is 0.10 m. Gas is injected radially from both the inner and outer electrodes at the midpoint of the coaxial accelerator. Magnetic measurements are made at $z = 0$ and 0.35 m. The arrows indicate the position of the current sheet and direction of current flow immediately after ionization (green) and after pinch formation (yellow). (b) ZaP with the perforated electrode extension. The perforated electrode section is 0.34-m long with eight large openings, resulting in ≈70% less conducting wall surface than the solid electrode section. Magnetic measurements are made at $z = 0$, 0.31, and 0.69 m. Optical and interferometry measurements are made in the perforated section.

TABLE I
ZAP OPERATING PARAMETERS

Parameter	Value
Accelerator Length (m)	1
Outer Electrode Radius (m)	0.10
Inner Electrode Radius (m)	0.05 or 0.08
Pinch Radius, a (m)	0.01
Pinch Length (m)	1
Peak Current (kA)	300-400
Electron Density (m^{-3})	10^{22} - 10^{23}
Temperature, T_e, T_i (eV)	75 - 125
Magnetic Field (T)	1-2
Pinch Duration (μs)	30-70

this paper, an additional section of outer electrode (0.34-m long) was added to ZaP, which is perforated with eight large openings, reducing the surface area of the conducting wall by ≈70%, as shown in Fig. 2. This modification prevents currents from flowing the azimuthal distance required to stabilize the $m = 1, 2, 3$ modes, which are experimentally monitored. The length of the perforated section is sufficient to evaluate its effect on instabilities as the optically-observed wavelength of instabilities in ZaP is on the order of the pinch radius (≈0.01 m) [38]. The growth rate of instabilities should increase if the conducting wall contributes to the stability of the plasma in ZaP. In particular, if flow shear is sufficient to provide stability, the effects of the conducting wall would be obscured. As the flow shear decreases, the effect of a conducting wall should become observable. If the stabilizing effect of the wall is due to azimuthal currents, then wall stabilization should be reduced in the case of the perforated wall. The perforated section of the outer electrode is many wavelengths away from the end electrodes. Therefore, in the measurement region the pinch can effectively be considered to have infinite length.

A. ZaP Diagnostics

Axial and azimuthal arrays of surface-mounted magnetic probes are located in the region of interest for both the solid and perforated electrodes. The solid electrode section has two azimuthal arrays located at $z = 0$ and 0.35 m and an axial array of magnetic probes every 0.05-m along this length through $z = 0.70$ m. The axial array is at a single azimuth on the experiment. The perforated electrode section has azimuthal arrays at $z = 0.31$ and 0.69 m with no axial array between them. The perforated section increases optical access for the use of interferometry and a fast-framing camera for visible light emissions. The surface-mounted magnetic probes are located on the outer conducting wall and measure the change in azimuthal magnetic field as a function of time, dB/dt. Analog integration of this signal provides the magnetic field evolution, $B(t)$. The axial probe array consists of probes located every 0.05 m along the length of the outer conducting wall from $z = -1.20$ to 0.70 m. This array determines the current distribution in the experiment. The azimuthal arrays consist of eight surface-mounted magnetic probes at a single axial location distributed every 45° on the outer conducting wall. Fourier decomposing the data from the azimuthal array determines the mode structure of the magnetic field, B_m, up to the $m = 3$ azimuthal mode number. The magnetic data indicate the average magnetic field ($m = 0$), radial displacement ($m = 1$), ellipticity ($m = 2$), and triangularity ($m = 3$) of the current centroid. The $m = 1$ mode is the fastest-growing and highest amplitude of the asymmetric modes and defines the stability criterion. When the normalized $m = 1$ mode (B_1/B_0) is <0.2, the radial displacement of the current centroid from the machine axis is <0.01 m [38]. The ZaP pulses exhibit a period of time during which this normalized value drops below 0.2 and the frequency of the magnetic fluctuations decreases. This is considered the stable, or quiescent, period.

A multichord helium–neon, Mach–Zehnder, heterodyne, and quadrature interferometer measures the chord-integrated density at two locations in the perforated section at different impact parameters providing a measure of the density gradient.

An Imacon 790 fast-framing camera with a 1 μs frame rate takes images of visible light emission as a function of time in the perforated electrode section. These images aid in the interpretation of the size, displacement, and stability of the pinch. The images are compared with the data from interferometry and magnetic probe arrays to evaluate diagnostic consistency.

IV. LINEAR STABILITY ANALYSIS

A method following from [17] and [35] was used to calculate the theoretical linear growth rates. This method solves linearized ideal magnetohydrodynamics (MHD) equations as an eigenvalue problem, resulting in a pair of coupled first order differential equations for the perturbed total pressure p^* and the radial displacement ξ_r

$$Xr\frac{\partial p^*}{\partial r} + C_{11}p^* + C_{12}(r\xi_r) = 0 \tag{2}$$

$$Xr\frac{\partial (r\xi_r)}{\partial r} + C_{21}p^* + C_{22}(r\xi_r) = 0 \tag{3}$$

where r is the radial distance and the displacement is assumed to have the form $\xi_r = \exp(\gamma t - ikz)$

$$p^* = 2\frac{B_\theta^2}{\mu_0}\frac{\xi_r}{r} - \frac{\rho\gamma^2}{Y}\nabla\cdot\xi_r \tag{4}$$

$$Y = \frac{\rho^2\gamma^4}{X\Gamma p + \rho\gamma^2 B_\theta^2/\mu_0} \tag{5}$$

$$X = \rho\gamma^2 + \frac{F^2}{\mu_0} \tag{6}$$

$$F = \frac{m}{r}B_\theta \tag{7}$$

$$C_{11} = 2\left(\frac{F^2}{\mu_0} + Y\frac{B_\theta^2}{\mu_0}\right) \tag{8}$$

$$C_{12} = X^2 - 2X\frac{B_\theta}{\mu_0}\frac{\partial(B_\theta/r)}{\partial r} - 2C_{11}\frac{B_\theta^2}{r^2\mu_0} \tag{9}$$

$$C_{21} = m^2 + k_z^2 r^2 + r^2 Y \tag{10}$$

$$C_{22} = -C_{11} \tag{11}$$

$\Gamma = 5/3$ is the ratio of specific heats, m is the azimuthal mode number, and k_z is the axial wavenumber. The boundary conditions [17] used for the $m = 1$ kink mode are

$$\xi_r|_{r=r_{\text{wall}}} = 0 \tag{12}$$

$$\left.\frac{\partial\xi_r}{\partial r}\right|_{r=0} = 0 \tag{13}$$

which corresponds to no displacement at the outer rigid wall (12) and a continuous displacement across the axis (13). In this analysis, the shear flow is assumed to be zero (similar to $\kappa = 0$ case in [17]). The eigenvalue problem defined by the differential equations (2) and (3) and the boundary conditions (12) and (13) are solved using a shooting method. This yields a real eigenvalue γ^2, where if γ^2 is greater then zero, the mode is unstable and the growth rate is γ. Otherwise γ^2 is <0 and this represents a stable oscillation with a frequency $\omega = -i\gamma$. Growth rates were calculated for a variety of conditions and then compared with nonlinear simulation results; these comparisons are presented in Section V-E.

V. SIMULATIONS OF A Z-PINCH

The $m = 1$ kink mode in a Z-pinch was modeled using the multiblock features of the HiFi code. The multiblock formulation of HiFi joins a collection of structured meshes, called blocks, into one single multiblock computational domain. This allows for globally unstructured meshes with geometries not possible with a single structured block. A straight circular cylindrical geometry [Fig. 3(a)] composed of five blocks was used to model a periodic Z-pinch and verify the kink mode growth rates found with the linear stability analysis. Simulations with a more complex nonaxisymmetric geometry with 76 blocks were also performed [Fig. 3(b)]. In each of the cases, the number of blocks used is to minimize grid distortions. More detail of the block configuration is provided in [39]. The 76 block geometry represents a perforated section of conducting wall similar to the outer electrode of the ZaP experiment [40]. The space behind the perforated electrode has been excluded in this case because it would be significantly more complex without much gain to the simulation. The growth rates for the perforated geometry are also compared with results obtained from the linear stability analysis.

A. MHD Model

A viscous, hyper-resistive MHD model with isotropic heat conduction in 3-D Cartesian coordinates provides the basis for performing the nonlinear simulations. The equations are

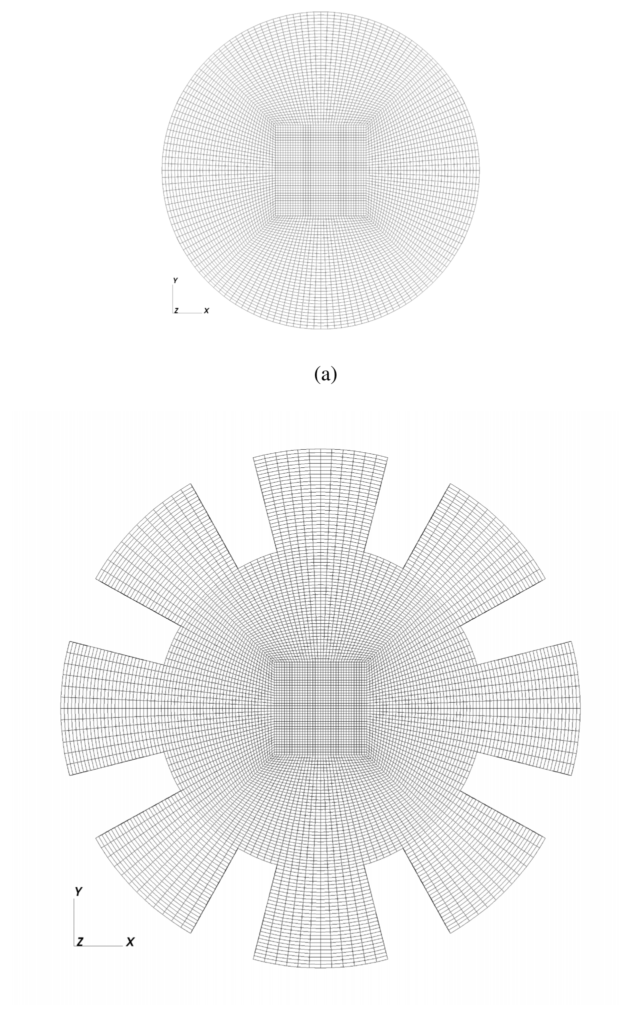

(a)

(b)

Fig. 3. Cross sections of the straight cylinder and cylinder with extrusions geometries. (a) 5 blocks. (b) 76 blocks.

written in flux-source form as

$$\frac{\partial}{\partial t}\begin{bmatrix}\rho\\ \rho\vec{v}\\ \vec{A}\\ \frac{1}{\Gamma-1}p\\ 0\end{bmatrix}+\nabla\cdot\begin{bmatrix}\rho\vec{v}\\ \rho\vec{v}\vec{v}+p\mathbf{I}-\mu\nabla\vec{v}\\ -\nu\nabla\vec{j}\\ \frac{\Gamma}{\Gamma-1}p\vec{v}-\kappa\nabla T\\ (\nabla\cdot\vec{A})\mathbf{I}-\nabla\vec{A}\end{bmatrix}=\begin{bmatrix}0\\ \vec{j}\times\vec{B}\\ \vec{v}\times\vec{B}-\eta\vec{j}\\ (\vec{v}\cdot\nabla p+\eta\vec{j}\cdot\vec{j}+\mu(\nabla\vec{v}:\nabla\vec{v}))\\ \vec{j}\end{bmatrix} \tag{14}$$

where $\mathbf{I}$ is the identity matrix, ρ is mass density, $\vec{v}$ is fluid velocity, $\vec{A}$ is magnetic vector potential, and p is pressure. The symbol: is the tensor double dot product operator defined as

$$\nabla\vec{v}:\nabla\vec{v}=\sum_{i=1}^{3}\sum_{j=1}^{3}\nabla v_{ij}\nabla v_{ji} \tag{15}$$

resulting in a scalar value. The dissipative parameters μ, η, κ, and ν are viscosity, resistivity, isotropic heat conduction, and hyper-resistivity, respectively. These parameters are defined in terms of their primitive variables as: $\mu \rightarrow \mu/(\rho v L) = 1/Re$, $\eta \rightarrow \eta/(\mu_0 v L) = 1/S$, $\kappa \rightarrow \kappa/(\rho v L) = 1/Pr$, and $\nu \rightarrow \nu/(\mu_0 v L^3)$, where L is the characteristic length scale. These expressions are the inverse of common dimensionless parameters, such as Reynolds, Lundquist, and Prandtl numbers. The hyper-resistive parameter, ν is a dimensionless number, and in these simulations provides high-order dissipation for numerical stability. This is useful for damping high-frequency noise in the current density, $\vec{j}$. The dimensionless numbers allow the simulations to be expressed in physical units (e.g., MKS-eV) by defining the initial condition and dissipative parameter magnitudes accordingly. In addition, the magnetic field intensity, $\vec{B} = \nabla \times \vec{A}$, current density, $\vec{j} = \nabla \times \nabla \times \vec{A}$, and temperature, $T \propto p/\rho$, are defined to complete the model.

B. Bennett Pinch Initial Conditions

A Bennett Z-pinch equilibrium is used as the equilibrium for the linear stability analysis and for the nonlinear simulations as the initial condition and is a solution to the force balance (1). The form of the equilibrium is

$$B_\theta = \frac{\mu_0 I_0}{2\pi}\frac{r}{r^2+a^2} \tag{16}$$

$$j_z = \frac{I_0}{\pi}\frac{a^2}{(r^2+a^2)^2} \tag{17}$$

$$p = \frac{\mu_0 I_0^2}{8\pi^2}\frac{a^2}{(r^2+a^2)^2} \tag{18}$$

where I_0 is the total current and a is the characteristic plasma pinch radius [29]. The Bennett equilibrium is a well-studied analytic profile that is similar to observed ZaP equilibria [41], which have a Lorentzian density profile ($n(r) \propto 1/(r^2+a^2)$) and a broader temperature profile than a Lorentzian, producing a pressure profile that is broader than a Bennett pressure profile, but fairly similar. To use the Bennett equilibrium as the initial equilibrium with (14), the magnetic field must be represented as vector potential. Since $\vec{B} = \nabla \times \vec{A}$, (16) can be integrated with respect to r

$$A_z = \int \frac{\mu_0 I_0}{2\pi}\frac{r}{r^2+a^2}dr = -\frac{\mu_0 I_0}{4\pi}\log[r^2+a^2]. \tag{19}$$

These equations for A_z, j_z, and p can be used as the initial condition, along with values for density, ρ, and momentum, $\rho\vec{v}$. The fluid momentum is initialized to zero with a small perturbation to initiate the $m = 1$ kink mode growth. The perturbation has the form

$$\rho v_y = \hat{\delta}[\cos(2\pi z/l_z)e^{-r^2/r_0^2}] \tag{20}$$

where $\hat{\delta}$ is the normalized magnitude of the perturbation, l_z is the axial wavelength of the pinch, at $r_0 = 0.03$ m limits the radial extent of the perturbation to ensure the perturbation vanishes at the radial boundary at $r = r_{\text{wall}} = 0.10$ m. A perturbation velocity normalized by the

Alfvén speed of $v_y/V_A = 7.25 \times 10^{-9}$ is given and is small enough that the dynamics remain in the linear phase throughout the simulation. This linear growth can then be compared with growth rates calculated from a linear stability analysis. For these simulations, conditions that closely match the operating parameters of the ZaP experiment were used (see Table I). The ZaP experiment pinch has a radius of $a = 0.01$ m, a number density $n = 10^{23}$ m^{-3}, a magnetic field strength of $B = 2$ T, and the outer conducting wall radius $r = 0.10$ m. In these simulations, a hydrogen plasma was assumed, so the density is $\rho = nM_p = 1.6726 \times 10^{-4}$ kg/m^3, where $M_p = 1.6726 \times 10^{-27}$ kg is the mass of a proton.

C. Boundary Conditions

The boundary conditions applied to the fluid velocity are perfect slip

$$\nabla_{\hat{n}} v_{\hat{t}} = 0 \tag{21}$$

$$v_{\hat{n}} = 0 \tag{22}$$

where $\nabla_{\hat{n}}$ is the normal gradient operator, $v_{\hat{t}}$ is the tangential fluid velocity, and $v_{\hat{n}}$ is the normal fluid velocity. These conditions prevent boundary layers by applying free-slip wall conditions and are justified by the low viscosity of the plasma near the wall. The magnitude of fluid flows in the simulations are small enough that boundary layers do not form. A conducting wall boundary condition is applied

$$\frac{\partial A_{\hat{t}}}{\partial t} = -E_{\hat{t}} = 0 \tag{23}$$

where $A_{\hat{t}}$ is the tangential vector potential and $E_{\hat{t}}$ is the tangential electric field. In cylindrical coordinates

$$\nabla \cdot \vec{A} = \frac{1}{r}\frac{\partial}{\partial r}(rA_r) + \frac{1}{r}\frac{\partial A_\phi}{\partial \phi} + \frac{\partial A_z}{\partial z} = 0. \tag{24}$$

If this divergence condition is also applied at the boundary it ensures that the respective A_r and A_ϕ terms go to zero at the boundary, regardless of the orientation of the boundary wall. This condition enforces that the conducting wall boundary condition is compatible with the sharp corners that exist in the extrusion geometry. The boundary condition for the temperature at the wall is given by

$$\frac{\partial}{\partial \hat{n}}(p/\rho) = 0 \tag{25}$$

where $T \propto p/\rho$. This condition allows the plasma to be wall-supported in the case with a diffuse Bennett pinch profile.

D. Optimization of Simulation

Viscosity, resistivity, hyper-resistivity, and isotropic heat conduction are included in the equation model described in (14). The ideal MHD linear stability analysis does not include dissipative terms, and therefore they are minimized in the Z-pinch simulations to make a good comparison. A small amount of both viscosity and hyper-resistivity are included that do not significantly impact the solution and provide numerical stabilization. The hyper-resistivity as opposed to resistivity is particularly helpful in this case because it dampens the high-frequency noise and minimally impacts the lower frequency solution. The goal is to keep the dissipative parameters small and hyper-resistivity is effective at damping the high-frequency current yielding sufficient numerical stability of the magnetics, while preserving the macroscopic solution. In addition, the spatial and temporal resolutions are tuned such that the growth rates have converged.

TABLE II

NORMALIZED GROWTH RATES CALCULATED FROM A NUMERICAL SIMULATION $(\gamma/k_z V_A)_n$ OF A Z-PINCH $m = 1$ KINK IN A STRAIGHT CIRCULAR CYLINDRICAL GEOMETRY, $r_{\text{wall}} = 0.10$ m, COMPARED WITH GROWTH RATES CALCULATED FROM A LINEAR STABILITY ANALYSIS $(\gamma/k_z V_A)_{ls}$. SEVERAL VALUES FOR THE CHARACTERISTIC PINCH SIZE a ARE COMPARED WITH VALUES OF $k_z a = \pi/4, \pi/2$, AND π

$k_z a$	a (m)	$(\gamma/k_z V_A)_n$	$(\gamma/k_z V_A)_{ls}$	%error
$\pi/4$	0.010	0.57030	0.58405	2.35
	0.015	0.57797	0.58405	1.04
	0.020	0.57326	0.58396	1.83
	0.030	0.56700	0.57787	1.88
	0.050	0.52260	0.54035	3.29
	0.050	0.42850	0.43274	0.98
$\pi/2$	0.010	0.50598	0.52125	2.93
	0.015	0.51035	0.52125	2.09
	0.020	0.51313	0.52125	1.56
	0.030	0.51590	0.52123	1.03
	0.040	0.51748	0.52050	0.58
	0.050	0.51323	0.51604	0.54
	0.060	0.49969	0.50271	0.60
	0.070	0.47282	0.47533	0.53
	0.080	0.42250	0.42948	1.63
π	0.010	0.36201	0.38424	5.79
	0.015	0.36875	0.38424	4.03
	0.020	0.37255	0.38424	3.04
	0.030	0.37669	0.38424	1.97
	0.040	0.37834	0.38424	1.54
	0.050	0.37971	0.38423	1.17
	0.060	0.37982	0.38406	1.11
	0.070	0.37923	0.38335	1.07
	0.080	0.37794	0.38137	0.90

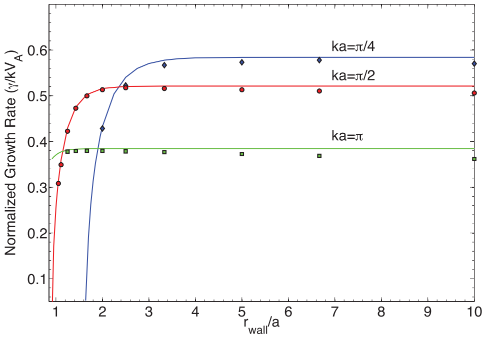

Fig. 4. Normalized growth rates computed from a linear stability analysis (lines) and from HiFi simulations (markers) for various values of r_{wall}/a while holding constant $k_z a = \pi/4, \pi/2$, and π.

E. Circular Cylinder Geometry

A straight circular cylindrical geometry is used to study the Z-pinch $m = 1$ kink mode. The mesh cross section is shown in Fig. 3(a). Growth rates calculated from numerical simulations for several pinch conditions are shown in Table II and are compared with the results from the linear stability analysis. In addition, Fig. 4 shows results from a linear stability analysis

TABLE III

NORMALIZED GROWTH RATES CALCULATED IN A STRAIGHT CIRCULAR CYLINDRICAL GEOMETRY COMPARED WITH A CYLINDER WITH EXTRUSIONS. SEVERAL VALUES FOR THE CHARACTERISTIC PINCH SIZE, a, ARE COMPARED, WHILE KEEPING $k_z a = \pi/2$ AND $r_{\text{wall}} = 0.10$ m

a (m)	$(\gamma/k_z V_A)_n$	$(\gamma/k_z V_A)_n$ (ext.)
0.01	0.50598	0.50651
0.04	0.51748	0.51669
0.06	0.49969	0.50136
0.08	0.42250	0.43661

while holding $k_z a$ fixed at $\pi/4$, $\pi/2$, and π and varying r_{wall}/a. Notice that for all three cases plotted, the effect of wall stabilization diminishes above some value of r_{wall}/a. For instance in the case with $k_z a = \pi/4$ wall stabilization only occurs when r_{wall}/a is less than about four, and has no stabilizing effect when the ratio is larger. With larger $k_z a$ the effect of wall stabilization is reduced further, even for large characteristic plasma radii (i.e., with $k_z a = \pi$ and $r_{\text{wall}}/a < 1.4$ for stability).

F. Modified Outer Electrode Geometry

As described in Section III, a perforated section of the surrounding wall was installed in the ZaP experiment. To simulate this geometry, a multiblock grid was designed with a domain that extrudes into the openings of the conducting wall. The perforations in the conducting wall mean that plasma is free to expand radially out of the original cylindrical volume and further into the vacuum vessel. To represent this in a computational domain, extrusions were added to the cylindrical geometry such that in the simulation the plasma has the ability to move into these regions. The depth of the extrusions are long enough such that the plasma interaction with the ends of the extrusions is minimal. The azimuthal surface currents are impeded at $r \geq r_{\text{wall}}$, especially with the low-plasma densities expected with the diffuse Bennett pinch profile. In the axisymmetric case, the surface currents were in the range 1×10^{-9} to 3.523×10^{-2} A/m for pinch sizes $a = 0.01$ and 0.08 m, respectively. With the addition of the extrusions the current decreased to roughly 25% of the axisymmetric case for a pinch size of $a = 0.08$ m.

Simulations with the modified outer electrode geometry were performed with a range of wall radius to characteristic plasma size ratios like the straight cylinder results. The pressure, current density, and magnetic field profiles are comparable with the ZaP experiment, and the case with $a = 0.01$ m most resembles the characteristic pinch radius seen in the experiment. Additional larger pinch sizes were simulated to better understand wall stabilization of the $m = 1$ kink mode in a Z-pinch.

The growth rates are impacted by the inclusion of the extrusions to the computational domain, however, the effect is minimal as is evident in Table III and Figs. 5 and 6. Simulation results of the fully developed kink mode in both the axisymmetric cylinder and the cylinder with extrusions are shown in Fig. 5. Table III shows the results of the normalized growth rates computed from HiFi simulations for both geometries and Fig. 6 shows the kinetic energy for cases with and without extrusions as a function of dimensionless normalized time τ. The time τ is normalized by the time it takes to reach the end of the linear growth phase, which is when the kinetic energy has saturated and is no longer linear in log space. All results have $k_z a = \pi/2$.

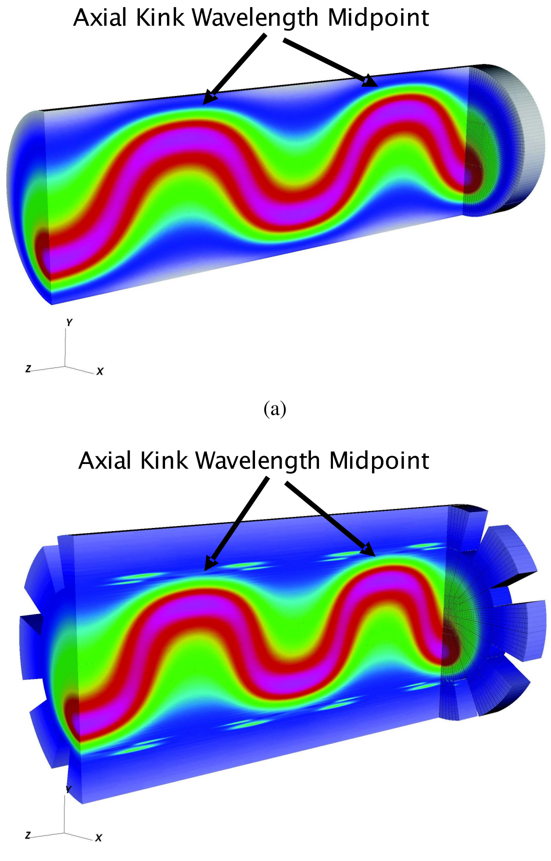

(a)

(b)

Fig. 5. Pressure, p, in both the cylinder and cylinder with extrusions with a characteristic plasma pinch radius of $a = 0.08$ m at $\tau = 23.8$, where τ is a dimensionless normalized time. Domain is duplicated in the axial direction for visual clarity. (a) 5 block cylinder. (b) 76 block cylinder with extrusions.

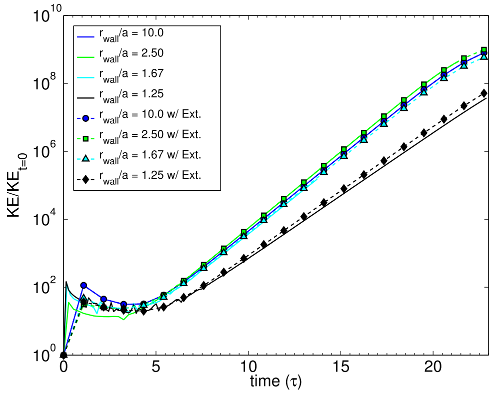

Fig. 6. Normalized kinetic energy computed from HiFi simulations for various values of r_{wall}/a for $k_z a = \pi/2$ for geometries with and without extrusions.

Notice with $r_{\text{wall}}/a = 1.25$, early in the linear growth phase at $\tau = 10$, the case with extrusions diverges from the

TABLE IV

PRESSURE VALUES FOR DIFFERENT PINCH SIZES, a, AT THE KINK WAVELENGTH MIDPOINT AT GAP AND ROD AZIMUTHAL LOCATIONS. RATIOS OF THE PRESSURE AT THE GAP AND ROD LOCATIONS ARE ALSO SHOWN. ALL RESULTS ARE $\tau = 23.2$, WHICH IS THE END OF THE LINEAR GROWTH PHASE FOR THE CASE WITH $k_z a = \pi/2$ AND $r_{\text{wall}} = 0.10$ m, WHERE τ IS A DIMENSIONLESS NORMALIZED TIME

a (m)	p_{gap}	p_{gap}^{ext}	p_{rod}	p_{rod}^{ext}	$\frac{p_{gap}}{p_{rod}}$	$\frac{p_{gap}^{ext}}{p_{rod}^{ext}}$
0.01	0.64×10^3	0.62×10^3	0.64×10^3	0.64×10^3	1.00	0.97
0.04	0.31×10^6	0.23×10^6	0.23×10^6	0.15×10^6	1.36	1.52
0.06	1.01×10^6	0.99×10^6	0.81×10^6	0.52×10^6	1.25	1.92
0.08	1.22×10^6	1.20×10^6	1.18×10^6	1.05×10^6	1.03	1.14

straight cylinder case. Numerical results show that the added extrusions increase the kinetic energy growth rates. Examining the pressure at the radial boundary shows a clearer distinction between the case with and without extrusions. Table IV shows a comparison of pressure values at the axial kink wavelength midpoint (kink peak in positive $\hat{y}$ direction) at two azimuthal locations for the cases with and without extrusions. The two azimuthal values are $\theta_{\text{gap}} = \pi/2$, and $\theta_{\text{rod}} = 3\pi/8$ and are locations for the center of a gap and rod, respectively. The gap location is the center of an extrusion and the rod location is the center of a remaining wall section. Fig. 6 shows the kinetic energy for cases with and without extrusions.

The addition of the extrusions reduces the plasma pressure experienced at both the gap and rod radial wall locations. As the pinch size increases, the ratio of the pressure at the gap to rod locations initially increases, and then decreases with larger pinch sizes. When the pinch size is a larger fraction of the cylindrical volume, the wall plays a more important role, which is consistent with the linear analysis. Fig. 7 shows pressure slices at the midpoint of the kink axial wavelength for $k_z a = \pi/2$ at time $\tau = 23.2$. As predicted by linear stability analysis, when the pinch size is large enough, there is a stabilizing effect on the plasma. Even in the case with a perforated wall, the rods have some stabilizing effect depending on their relative size with respect to the pinch. Notice that for the case with $a = 0.06$ m [Fig. 7(f)] the pinch size is large enough to have interactions with the wall and perforations, but not broad enough to interact with many of the rod locations. It is expected that this effect will vary depending on the width and number of perforations compared with the pinch size.

VI. EXPERIMENTAL EVIDENCE OF THE ABSENCE OF WALL STABILIZATION

The effects of the conducting wall on stability were investigated by operating ZaP with the same capacitor bank energy, gas injection characteristics, and coaxial accelerator geometry with and without the perforated conducting wall section. Similar operating conditions and magnetic data for both configurations would indicate similar equilibrium and flow shear characteristics, isolating the effect of the perforated wall.

Table I shows that the ratio r_w/a for ZaP is in the range for which simulations indicate that the conducting wall should have no effect. As mentioned, if the flow shear is sufficient the stabilizing effects of a conducting wall would be obscured. As flow shear decreases, the growth of instabilities is theoretically predicted to increase. Reduced growth of instabilities would be apparent by comparing the pinch behavior of the solid conducting wall with the perforated conducting wall as flow shear decreases if the conducting wall is contributing to stability.

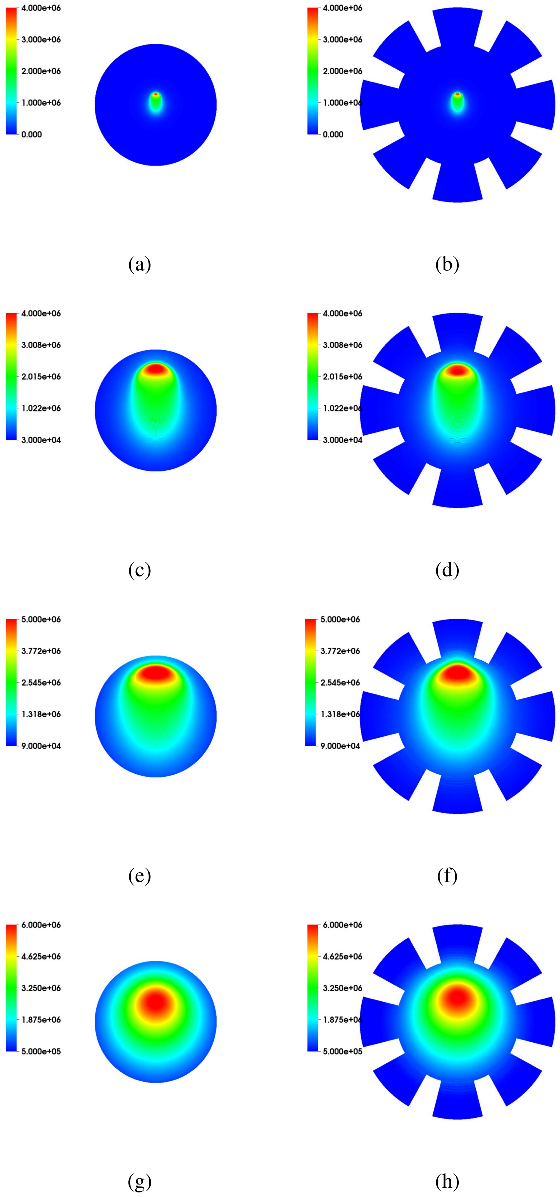

(a) (b)

(c) (d)

(e) (f)

(g) (h)

Fig. 7. Pressure profiles at the midpoint of the axial kink wavelength for characteristic plasma sizes of $a = 0.01$, 0.04, 0.06, and 0.08 m with and without radial extrusions. All figures are at time $\tau = 23.2$, where τ is a dimensionless normalized time and are normalized by the axial wavenumber times the Alfvén speed $k_z V_A$. (a) $a = 0.01$ m. (b) $a = 0.01$ m. (c) $a = 0.04$ m. (d) $a = 0.04$ m. (e) $a = 0.06$ m. (f) $a = 0.06$ m. (g) $a = 0.08$ m. (h) $a = 0.08$ m.

For the data shown in Figs. 8 and 9, the experimental conditions were a 0.05-m outer radius inner electrode, a 0.10-m inner radius conducting wall and a 7-kV capacitor bank voltage on eight 180-μF capacitors. The peak current in the experiment was $I \approx 200$ kA.

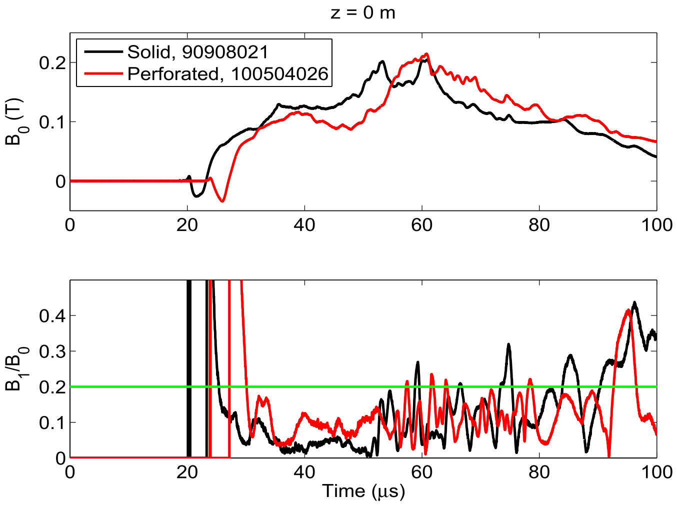

Fig. 8. Fourier mode data from the azimuthal magnetic probe array located at $z = 0$ m with and without the perforated conducting wall section. Top plot is average magnetic field as a function of time, bottom plot is normalized $m = 1$ magnetic fluctuations as a function of time. The horizontal line in the bottom plot represents the ZaP stability definition of $B_1/B_0 \leq 0.2$.

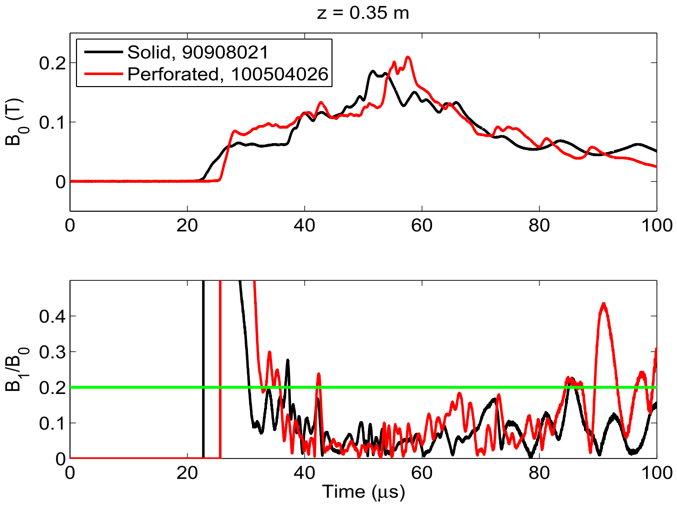

Fig. 9. Fourier mode data from the azimuthal magnetic probe array located at $z = 0.35$ and 0.31 m with and without the perforated conducting wall section.

Fig. 8 shows the magnetic data for two different pulses, one with the perforated section and one without the perforated section at the axial location $z = 0$ m, which is ≈0.35-m upstream of the perforated conducting wall section. The top plot is the average magnetic field and the bottom plot is the normalized $m = 1$ magnetic fluctuations. The horizontal green line in the bottom plot indicates the ZaP stability definition of $B_1/B_0 \leq 0.2$. The error bars for all magnetic data presented are on the order of 10^{-3} T or less [37], [42]. The data indicate that for similar operating conditions the magnetic data at $z = 0$ m is similar with and without the perforated conducting wall section. The magnitude during the quiescent period has a plateau of ≈0.1 T at the wall for ≈20 μs before an increase in field up to 0.2 T. During this plateau, the normalized mode data exhibits magnitude below 0.2, indicating a well-centered pinch for an extended period of time ($t \approx$ 30–50 μs). The behavior is observed for pulses with and without the perforated conducting wall section. The transition to instability due to reduction in sheared flow occurs at ≈50 μs as the magnitude and frequency of the normalized magnetic mode data increases substantially, with the magnitude increasing above 0.2 within 3–5 μs. This similar behavior suggests that the plasma equilibrium and flow shear conditions are similar for both pulses and the addition of the perforated conducting wall section does not significantly affect the overall pinch behavior.

Fig. 9 shows the magnetic mode data at $z = 0.35$ m for the solid conducting wall section and $z = 0.31$ m for the perforated conducting wall section for the same pulses as Fig. 8. The difference in axial location of the probe array between the two configurations is not considered to change the interpretation of the data, due to the observed axial uniformity of the plasma which is described later in this section. These data indicate that for similar experimental operating conditions, the average magnetic field and the stability characteristics are similar in both the perforated conducting wall section and the solid cylindrical section.

The average magnetic fields exhibit similar magnitudes and waveforms with a gradual increase from 0.08 to 0.2 T over ≈30 μs. Both pulses indicate a well-centered pinch for an extended period of time, from $t \approx$ 42 to 85 μs as observed on the normalized magnetic mode data. Both pulses exhibit a similar pinch formation period indicated by the high-frequency oscillations and sharp decrease in the magnitude of the normalized magnetic mode data before $t \approx 42$ μs. The end of the quiescent period at $t \approx 85$ μs, which corresponds to the decay of sheared flow, is when differences in the stability characteristics would be observed if the conducting wall were having a significant effect on the stability. The data showing this transition to instability for both pulses are nearly identical, suggesting that the removal of conducting wall material has no effect on the pinch stability.

The difference in quiescent period lengths between $z = 0$ m (≈25 μs) and $z = 0.35$ m (≈43 μs), as shown in Figs. 8 and 9, is a consequence of the propagation of sheared flow in the experiment and its effects on stability. Plasma initially assembles near $z = 0$ m and a high-velocity sheared flow is established early in the quiescent period. This flow propagates downstream quickly, 7×10^4 m/s based on a 5-μs difference in plasma arrival times between the two locations (0.35 m). The flow velocity decays toward the end of the quiescent period, 1×10^4 m/s (0.35 m in ≈35 μs) resulting in a longer quiescent period at $z = 0.35$ m. These axial velocities are in good agreement with previous velocity measurements based on Doppler shift of impurity radiation [23]. This behavior also justifies the use of the $z = 0.31$-m probe array to interpret results in the perforated region which is 0.09-m upstream.

A statistical investigation of shot-to-shot variations for the conditions in Fig. 9 was considered by computing the standard deviation as a function of time for seven shots at identical conditions for both the solid and perforated wall conditions. Values of B_0 for both wall conditions have standard deviations of <20% throughout the quiescent period. The values of B_1/B_0 for the perforated electrode have standard deviations between 0.02 and 0.05 during the quiescent period, increasing from 0.05 to 0.08 after the quiescent period ends. The solid

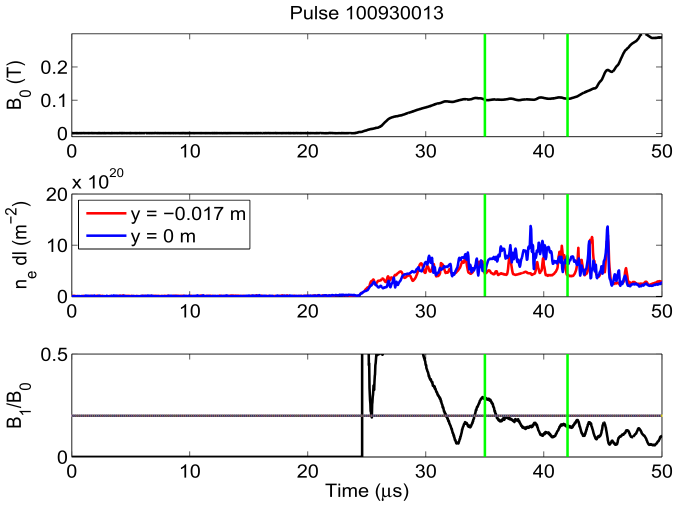

Fig. 10. Fourier mode data from the azimuthal magnetic probe array located at $z = 0.31$ m and 2-chord interferometry at $z = 0.40$ m, green vertical lines indicate the beginning and end of optical images observed in Fig. 11. Top plot is average magnetic field as a function of time. Middle plot is chord-integrated data from two chords of interferometry located at $y = 0$ and -0.017 m. Bottom plot is normalized $m = 1$ magnetic fluctuations.

electrode data have standard deviations from 0.02 to 0.07 during the quiescent period, increasing to a range of 0.04–0.1 after the quiescent period ends. The increase in standard deviation after the quiescent period is consistent with the unpredictability associated with instability and the low standard-deviation during the quiescent period suggests the behavior shown in Fig. 9 during the quiescent period is representative of the plasma behavior.

Results from multiple capacitor bank configurations provide further evidence that the stability characteristics in the perforated section are consistent across muliple operating conditions. Fig. 10 shows the magnetic mode data at $z = 0.31$ m and interferometry data at two impact parameters at $z = 0.40$ m in the perforated section. The operating conditions for this pulse are a 0.05-m radius inner electrode with a 6-kV capacitor bank voltage on sixteen 180-μF capacitors. The peak current for this configuration was $I \approx 250$ kA. These data indicate that during periods of low-magnetic fluctuations, a well-defined pinch is formed beginning at $t \approx 36$ μs. The central interferometry chord ($y = 0$ m) measures increased chord-integrated density when the normalized $m = 1$ data falls below the stability threshold and the off-center chord ($y = -0.017$ m) remains at a lower level indicative of a diffuse plasma surrounding a pinch. Prior to $t \approx 36$ μs, both chords measure a similar chord-integrated density because this is during the formation process and a coherent pinch structure has not yet been formed. After $\approx$42 μs, the central interferometry chord returns to background levels while the quiescent period continues. This is due to pinch moving in the positive y-direction (calculated from B_1/B_0 data) above and out of view of the interferometer chords and not due to increasing instabilities. Error bars for interferometry data shown are on the order of 10^{19} m^{-2} [37].

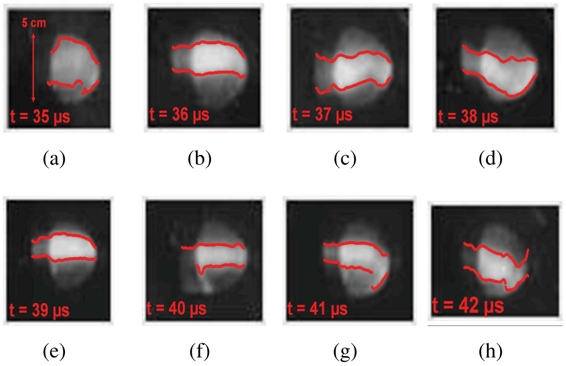

(a) (b) (c) (d)

(e) (f) (g) (h)

Fig. 11. Visible light images from Imacon 790 fast-framing camera with a 1-μs frame rate taken in the perforated conducting wall section for the pulse shown in Fig. 10. The images begin at 35 μs and end at 42 μs, plasma flow direction is from right to left. The red symbols indicate the boundaries of the pinch as a function of axial extent, calculated as the the point at which the intensity of the emission is 75% of the maximum value. (a) 35 μs. (b) 36 μs. (c) 37 μs. (d) 38 μs. (e) 39 μs. (f) 40 μs. (g) 41 μs. (h) 42 μs.

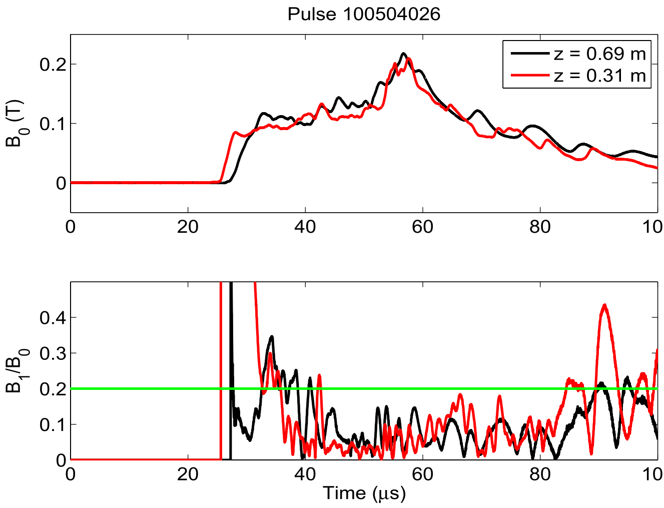

Fig. 12. Fourier mode data from the azimuthal magnetic probe arrays located at $z = 0.31$ and 0.69 m (upstream and downstream of the perforated conducting wall section).

The vertical green lines indicate the initial and final times for the fast-framing camera images shown in Fig. 11 taken in the perforated conducting wall section ($z = 0.40$ m). The first image is taken at 35 μs and the last image is taken at 42 μs with 1 μs between images. The red symbols indicate the boundaries of the pinch as a function of axial extent, calculated as the location at which the intensity of the emission is 75% of the maximum value. The direction of plasma flow in each image is from right to left. The images indicate a well-defined stable pinch. These data agree with the magnetic data and interferometry shown in Fig. 10. The optical images show a well-defined pinch during the periods in which magnetic fluctuations are low and a well-centered current centroid is observed and the central interferometer chord measures noticeably increased chord-integrated density during these times.

Further evidence of a confined, coherent pinch throughout the length of the perforated section is achieved with measurements of the axial magnetic uniformity. These measurements are made by comparing the magnitude of the magnetic field and magnetic fluctuations at the probe arrays upstream and downstream of the perforated conducting wall section

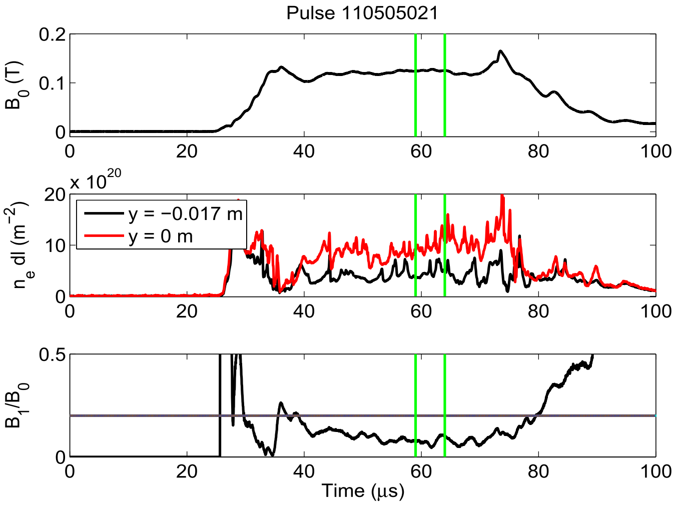

Fig. 13. Fourier mode data from the azimuthal magnetic probe array located at $z = 0.31$ m and 2-chord interferometry at $z = 0.40$ m for a 0.08-m radius inner electrode accelerator configuration, green vertical lines indicate the beginning and end of optical images observed in Fig. 14.

($z = 0.31$ and 0.69 m). These data are shown in Fig. 12 and indicate that the magnetic field at these widely spaced locations have similar magnitudes and waveforms, with a field value at the wall rising from 0.1 T until it peaks at 0.2 T and begins a gradual decay. The waveforms at both locations are nearly identical indicating little radial current loss from the pinch in the perforated conducting wall section. Normalized magnetic mode data are low at both locations from $t \approx 42$ to 82 μs. These data suggest a coherent axial structure to the plasma throughout the perforated electrode section, indicating that the magnetic probe arrays upstream and downstream are a valid measurement of the pinch behavior inside the perforated section.

The evidence of stability without the effects of a conducting wall in ZaP is invariant with changes in the coaxial accelerator configuration. The ZaP can optionally use a 0.08-m radius inner electrode in place of the more standard 0.05-m inner electrode. The data presented for the 0.08-m radius inner electrode are for a capacitor bank voltage of 6 kV on sixteen 180-μF capacitors. The peak current in the experiment for these configurations was $I \approx 400$ kA.

Diagnostics in the perforated conducting wall section consistently indicate a well-defined pinch structure that persists for an extended quiescent period for many different pulses with these operating conditions. Data from a single pulse will be shown.

Fig. 13 shows the magnetic data from the azimuthal magnetic probe array at $z = 0.31$ m and two chords of interferometry located in the perforated conducting wall section at $z = 0.40$ m. The data indicate that at the beginning of the quiescent period ($t \approx 40$ μs), the chord-integrated electron density from the central interferometry chord increases while the off-center chord remains at a lower level, indicating a well-formed pinch centered in the perforated electrode section. Similarly, as the quiescent period ends ($t \approx 79$ μs) both interferometer chords exhibit lower levels of chord-integrated density, indicating that a well-formed pinch is no longer in evidence.

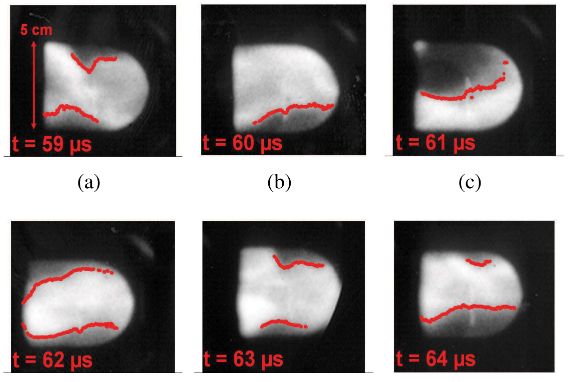

(a) (b) (c)

(d) (e) (f)

Fig. 14. Visible light images from Imacon 790 fast-framing camera with a 1-μs frame rate taken in the perforated conducting wall section for the pulse shown in Fig. 13. The images begin at 59 μs and end at 64 μs, plasma flow direction is from right to left. The red symbols indicate the boundaries of the pinch. (a) 59 μs. (b) 60 μs. (c) 61 μs. (d) 62 μs. (e) 63 μs. (f) 64 μs.

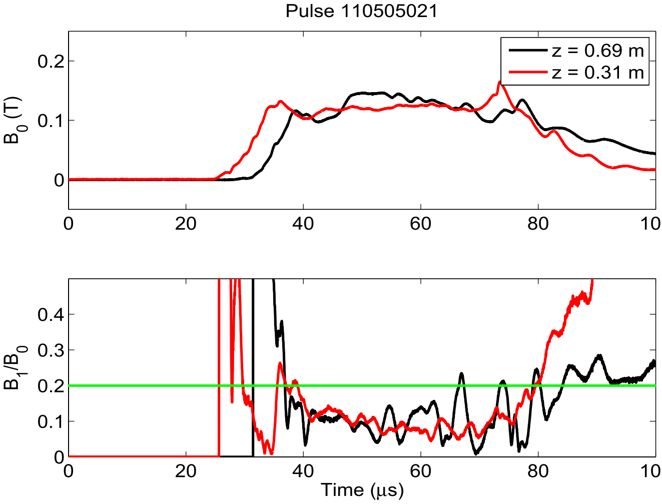

Fig. 15. Fourier mode data from the azimuthal magnetic probe arrays located at $z = 0.31$ and 0.69 m for the 0.08-m radius inner electrode configuration.

Fig. 14 shows visible light images in the perforated conducting wall section ($z = 0.40$ m) for the pulse shown in Fig. 13. The first image is taken at 59 μs and the last image is taken at 64 μs with 1 μs between images. The red symbols indicate the boundaries of the pinch. The direction of plasma flow is from right to left in each image. The images indicate a well-defined pinch structure that persists through the period of observation. In Fig. 14(b) and (c), only one side of the pinch is observed due to the optical extent of the openings in the conducting wall in some images. This limited view still suggests an axially coherent structure. These images are in agreement with the magnetic and interferometric data shown in Fig. 13 in which the central interferometry chord displays increased density and the normalized magnetic mode data indicates a well-centered current centroid.

This experimental configuration shows uniformity of the magnetic structure through the length of the perforated conducting wall section, similar to data for the 0.05-m diameter inner electrode. Fig. 15 shows data from the magnetic probe arrays upstream and downstream of the perforated conducting wall section. The data indicate that the magnitude and waveform of the magnetic field are similar at these widely-space locations with a long plateau of 0.1 T at the wall from $t \approx 40$ to 75 μs. This indicates little current loss from the pinch, which is indicative of a coherent axial structure during this time. In addition, the stability characteristics indicate a stable pinch from $t \approx 40$ to 65 μs at $z = 0.69$ m and from $t \approx 40$ to 80 μs at $z = 0.31$ m.

VII. CONCLUSION

In this paper, we have presented the results of a systematic experimental and numerical investigation of the effects of a conducting wall on the stability of a Z-pinch that supports the conclusion that a conducting wall must be in close proximity to the pinch boundary to provide a stabilizing effect and that a conducting wall does not have a discernible effect on the stability in the ZaP Flow Z-Pinch.

The Z-pinch simulations performed agree with the theoretical results obtained by a linear stability analysis, which is a promising verification of the HiFi code and the multiblock geometry framework. The discrepancy between theory and HiFi simulation results is mostly less than a few percent, showing a strong convergence of the results. The simulations using the cylinder with extrusion geometry further verify the code's abilities and make use of a more complex nonaxisymmetric multiblock geometry. The results obtained show how the extrusions affect the wall stabilization. No impact is seen when the pinch is small and far enough away from the boundary. When the pinch is large enough to interact with the boundary and on the order of the size of the extrusion gaps, the largest effect is found.

An experimental modification to the ZaP Flow Z-Pinch to evaluate the effects of a conducting wall on pinch stability was concurrently performed. A perforated outer conducting wall section was manufactured that has eight longitudinal slots that remove ≈70% of the outer conducting wall. The motivation for this modification was to reduce the extent of azimuthal current flow in the outer conductor. These currents must have the same mode structure as the plasma perturbations to produce a stabilizing effect. A conducting wall with eight longitudinal slots should prevent azimuthal currents that would stabilize the $m = 1, 2, 3$ modes. The conducting wall effects were isolated by operating the experiment with identical coaxial accelerator, capacitor bank, and gas injection conditions, producing similar equilibrium and flow shear conditions. Direct comparison of these operating conditions indicates that the conducting wall does not significantly affect pinch stability in ZaP. This is observed at the end of the quiescent period when flow shear decays. If the conducting wall azimuthal image currents provided stability, then the transition to instability would be faster for the perforated outer electrode configuration. Instead a coherent pinch structure is observed in the perforated conducting wall section that persists for lengths of time similar to that observed for a solid conducting wall section for multiple experimental configurations of accelerator geometry, capacitor bank, and gas injection characteristics.

Supporting data from magnetic probe arrays, optical images and interferometry indicate a stable, axially-uniform magnetic structure through the perforated conducting wall section with little current loss from the pinch that persists for times much longer than the instability growth time, which is on the order of 10 ns. The data indicate that modifying the geometry of the return current wall to reduce the azimuthal distance of current flow along the outer electrode circumference has no discernible effect on the stability of the Z-pinch and is further evidence that sheared axial flows are responsible for stability in ZaP.

ACKNOWLEDGMENT

The authors would like to thank the contributions of V. (Slava) Lukin and A. H. Glasser with their work in development of the HiFi code. They would also like to thank Slava's generous support with HiFi and in particular the initial Z-pinch simulations from which this research benefitted, and also the reviewers for their helpful suggestions and thorough evaluation of the manuscript.

REFERENCES

[1] H. Maecker, “Elektronendichte und temperatur in der säule des hochstromkohlebogens,” *Zeitschrift Phys.*, vol. 136, no. 2, pp. 119–136, 1953.
[2] J. B. Shumaker, “Arc source for high temperature gas studies,” *Rev. Sci. Instrum.*, vol. 32, no. 1, pp. 65–67, Jan. 1961.
[3] R. Jahn, *Physics of Electric Propulsion*. New York, NY, USA: Dover, 1968.
[4] R. John, S. Bennett, and J. F. Connors, “Arcjet engine performance: Experiment and theory,” *AIAA J.*, vol. 1, no. 11, pp. 2517–2525, 1963.
[5] L. Wallner and J. Czika, “NASA TN D-2868,” NASA, Washington, DC, USA, Tech. Rep. TN D-2868, 1965.
[6] V. R. Watson and E. B. Pegot, “Numerical calculations for the characteristics of a gas flowing axially through a constricted arc,” NASA, Washington, DC, USA, Tech. Rep. TN-D-4042, 1967.
[7] H. Stine, V. Watson, and C. Shepard, “Effect of axial flow on the behavior of the wall-constricted arc,” National Aeronautics and Space Administration, Ames Research Center, Moffett Field, CA, USA, Tech. Rep. TM X-54,065, 1964.
[8] R. A. Graves and W. L. Wells, “Preliminary study of a wall-stabilized constricted arc,” NASA, Washington, DC, USA, Tech. Rep. TM X-2700, 1973.
[9] R. C. Preston, “Spectroscopic studies of a plasma temperature and radiation standard based on a wall-stabilized arc,” *J. Quant. Spectrosc. Radiat. Transf.*, vol. 18, no. 3, pp. 337–360, 1977.
[10] K. E. Clark and R. G. Jahn, “The magnetoplasmadynamic arcjet,” *Astron. Acta*, vol. 13, pp. 315–325, Mar. 1967.
[11] R. Kilb, H. Hurwitz, Jr., and W. Westendorp, “Wall stabilization effects in theta-pinch configurations,” *Phys. Fluids*, vol. 5, no. 9, pp. 1131–1133, 1962.
[12] R. W. Kilb, H. Hurwitz, Jr., and W. F. Westendorp, “Wall stabilization effects in theta-pinch configurations,” *Phys. Fluids*, vol. 6, no. 9, pp. 1332–1337, 2004.
[13] F. A. Haas and J. A. Wesson, “Stability of the theta-pinch,” *Phys. Fluids*, vol. 9, no. 12, p. 2472, 1966.
[14] F. Haas and J. Wesson, “Stability of the theta-pinch. II,” *Phys. Fluids*, vol. 10, no. 10, p. 2245, 1967.
[15] B. Kadomtsev, *Reviews of Plasma Physics*, vol. 2, M. A. Leontovich, Ed. New York, NY, USA: Consultant Bureau, 1966, p. 153.
[16] F. Ribe, “LASL controlled thermonuclear research program. Progress report for a 12-month period ending December 1972,” Los Alamos Scientific Lab., Los Alamos, NM, USA, Tech. Rep. LA-7474-PR, 1973.
[17] U. Shumlak and C. W. Hartman, “Sheared flow stabilization of the m=1 kink mode in Z pinches,” *Phys. Rev. Lett.*, vol. 75, no. 18, pp. 3285–3288, 1995.
[18] J. P. Goedbloed, D. Pfirsch, and H. Tasso, “Instability of a pinch surrounded by a resistive wall,” *Nucl. Fusion*, vol. 12, no. 6, p. 649, 1972.
[19] E. J. Strait *et al.*, “Wall stabilization of high beta tokamak discharges in DIII-D,” *Phys. Rev. Lett.*, vol. 74, no. 13, p. 2483, 1995.

[20] T. Jarboe, "The spheromak confinement device," *Phys. Plasmas*, vol. 12, no. 5, p. 058103, 2005.

[21] M. N. Rosenbluth and M. N. Bussac, "MHD stability of spheromak," *Nucl. Fusion*, vol. 19, no. 4, p. 489, 1979.

[22] U. Shumlak, R. P. Golingo, B. A. Nelson, and D. J. Den Hartog, "Evidence of stabilization in the Z-pinch," *Phys. Rev. Lett.*, vol. 87, no. 20, p. 205005, 2001.

[23] U. Shumlak, B. A. Nelson, R. P. Golingo, S. L. Jackson, E. A. Crawford, and D. J. Den Hartog, "Sheared flow stabilization experiments in the ZaP flow Z pinch," *Phys. Plasmas*, vol. 10, no. 5, pp. 1683–1690, 2003.

[24] R. P. Golingo, "Modeling magnetic fields measured by surface probes embedded in a cylindrical flux conserver," *Rev. Sci. Instrum.*, vol. 78, no. 3, p. 033504, 2007.

[25] A. M. Garofalo *et al.*, "Stabilization of kink instabilities by eddy currents in a segmented wall and comparison with ideal MHD theory," *Nucl. Fusion*, vol. 38, no. 7, p. 1029, 1998.

[26] V. Lukin, A. H. Glasser, W. Lowrie, and E. Meier, "HiFi—Adaptive, implicit, high order finite element code for general multi-fluid applications," in *Proc. AAS/Solar Phys. Division Meeting*, vol. 40. May 2009.

[27] A. H. Glasser and X. Z. Tang, "The SEL macroscopic modeling code," *Comput. Phys. Commun.*, vol. 164, no. 1, pp. 237–243, 2004.

[28] T. Gray, V. S. Lukin, M. R. Brown, and C. D. Cothran, "Three-dimensional reconnection and relaxation of merging spheromak plasmas," *Phys. Plasmas*, vol. 17, no. 10, p. 102106, 2010.

[29] J. P. Freidberg, "Ideal magnetohydrodynamic theory of magnetic fusion systems," *Rev. Modern Phys.*, vol. 54, no. 3, p. 801, 1982.

[30] W. H. Bennett, "Magnetically self-focussing streams," *Phys. Rev.*, vol. 45, no. 12, p. 890, 1934.

[31] A. Bishop and U. A. E. Commission, *Project Sherwood: The US Program in Controlled Fusion*. Reading, MA, USA: Addison-Wesley, 1958.

[32] W. Newcomb, "Hydrodynamic stability of a diffuse linear pinch," *Ann. Phys.*, vol. 10, no. 2, pp. 232–267, 1960.

[33] R. J. Bickerton, "Pinch research," *Nucl. Fusion*, vol. 20, no. 9, p. 1072, 1980.

[34] U. Shumlak *et al.*, "Stabilization in the ZaP flow Z-pinch," *J. Fusion Energy*, vol. 28, no. 2, pp. 208–211, Jun. 2009.

[35] K. Appert, R. Gruber, and J. Vaclavik, "Continuous spectra of a cylindrical magnetohydrodynamic equilibrium," *Phys. Fluids*, vol. 17, no. 7, pp. 1471–1472, 1974.

[36] J. Marshall, "Performance of a hydromagnetic plasma gun," *Phys. Fluids*, vol. 3, no. 1, pp. 134–135, 1960.

[37] R. P. Golingo, U. Shumlak, and B. A. Nelson, "Formation of a sheared flow Z pinch," *Phys. Plasmas*, vol. 12, no. 6, p. 062505, 2005.

[38] U. Shumlak *et al.*, "Equilibrium, flow shear and stability measurements in the Z-pinch," *Nucl. Fusion*, vol. 49, no. 7, p. 075039, 2009.

[39] W. B. Lowrie, "Development and application of a multi-block high order finite element modeling code as an engineering design tool," Ph.D. dissertation, Dept. Aeronaut. and Astronaut., Univ. Washington, Seattle, WA, USA, 2011.

[40] U. Shumlak *et al.*, "The sheared-flow stabilized Z-pinch," *Fusion Sci. Technol.*, vol. 61, no. 1, p. 119, 2012.

[41] S. Knecht, "Comparison of electrode configurations on ZaP: Investigation of heating mechanisms in a flow Z-pinch," Ph.D. dissertation, Dept. Aeronaut. and Astronaut., Univ. Washington, Seattle, WA, USA, 2012.

[42] R. P. Golingo, "Formation of a sheared flow Z-pinch," Ph.D. dissertation, Dept. Aeronaut. and Astronaut., Univ. Washington, Seattle, WA, USA, 2003.

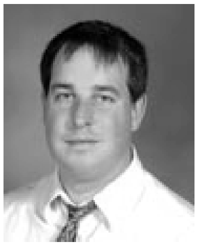

Sean D. Knecht received the B.S. degree in aerospace engineering from Pennsylvania State University, University Park, PA, USA, in 2005, and the M.S. and Ph.D. degrees in aeronautics and astronautics from the University of Washington, Seattle, WA, USA, in 2008 and 2012, respectively, where he studied experimental plasma physics on the ZaP Flow Z-Pinch Project.

He joined the Applied Research Laboratory, Pennsylvania State University, in 2012, where he is currently a Research Associate. His current research interests include low-temperature plasma physics, and nanoparticle-based photoacoustic biomedical imaging and detection.

Weston Lowrie was born in MA, USA, in 1979. He received the B.S. degree in mechanical engineering from Union College, New York, NY, USA, in 2003, and the M.S. and Ph.D. degrees in aerospace engineering from the University of Washington, in 2008 and 2011, respectively, where he studied computational fluid dynamics, plasma physics, and numerical methods.

He joined Applied Research Associates, Inc., Albuquerque, NM, USA, in 2012, where he is currently a Staff Scientist/Engineer, involved in modeling plasmas in the Earth's magnetosphere.

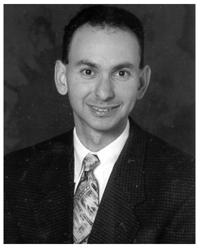

Uri Shumlak received the Ph.D. degree in nuclear engineering from the University of California, Berkeley, CA, USA, in 1992.

He was a National Research Council Post-Doctoral Fellow with the Air Force Research Laboratory, Albuquerque, NM, USA, where he developed the 3-D, resistive, MHD code, and MACH3. He is currently a Professor of Aeronautics and Astronautics and the Head of the ZaP Flow Z-Pinch Laboratory and the Computational Plasma Dynamics Group at the University of Washington, Seattle, WA, USA, where he was involved in the development of the WARPX plasma simulation code. He is also the Vice President of the University Fusion Association and a Chief Scientist with Zplasma, Inc., Seattle, WA, USA. His current research interests include plasma physics, innovative magnetic plasma confinement for fusion energy, high-energy density plasmas, astrophysics, extreme ultraviolet lithography, electric propulsion, and theoretical and computational plasma modeling.